Stacking as a key property for creating nanoparticles with tunable shape: The case of Squalenoyl-doxorubicin

Julie Mougin, Semen Yesylevskyy, Claudie Bourgaux, David Chapron, Jean-Philippe Michel, Franco Dosio, Barbara Stella, Christophe Ramseyer, Patrick Couvreur

ACS NANO

Cite This: ACS Nano 2019, 13, 12870−12879

www.acsnano.org

ARTICLE

Stacking as a Key Property for Creating Nanoparticles with Tunable Shape: The Case of Squalenoyl-Doxorubicin

Julie Mougin,[†] Semen O. Yesylevskyy,[‡,∥] Claudie Bourgaux,[†] David Chapron,[†] Jean-Philippe Michel,[†] Franco Dosio,[§] Barbara Stella,[§] Christophe Ramseyer,[∥] and Patrick Couvreur*[,†]

[†]Institut Galien Paris-Sud UMR CNRS 8612, Faculty of Pharmacy, Université Paris-Sud, Université Paris-Saclay, 92290 Châtenay-Malabry, France

[‡]Department of Physics of Biological Systems, Institute of Physics of the National Academy of Sciences of Ukraine, Prospect Nauky 46, 03028 Kyiv, Ukraine

[§]Dipartimento di Scienza e Tecnologia del Farmaco, Università degli Studi di Torino, 10125 Turin, Italy

[∥]Laboratoire Chrono Environnement UMR CNRS 6249, Université de Bourgogne Franche-Comté, 16 route de Gray, 25030 Besançon Cedex, France

Supporting Information

ABSTRACT: **The development of elongated nanoparticles for drug delivery is of growing interest in recent years, due to longer blood circulation and improved efficacy compared to spherical counterparts. Squalenoyl-doxorubicin (SQ-Dox) conjugate was previously shown to form elongated nanoparticles with improved therapeutic efficacy and decreased toxicity compared to free doxorubicin. By using experimental and computational techniques, we demonstrate here that the specific physical properties of SQ-Dox, which include stacking and electrostatic interactions of doxorubicin as well as hydrophobic interactions of squalene, are involved in the formation of nanoassemblies with diverse elongated structures. We show that SQ-Dox bioconjugate concentration, ionic strength, and anion nature can be used to modulate the shape and stiffness of SQ-Dox nanoparticles. As those parameters are involved in nanoparticle behavior in biological media, these findings could bring interesting opportunities for drug delivery and serve as an example for the design of original nanodrugs with stacking properties tuned for particular clinical purposes.**

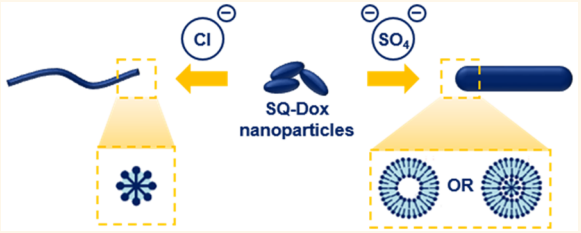

KEYWORDS: *cylindrical nanoparticles, elongated nanoparticles, squalene, doxorubicin, stacking, bioconjugate, nanomedicine*

Doxorubicin (Dox) is a widely used anticancer drug presenting a broad spectrum of activity but limited by dose-dependent and irreversible cardiotoxicity.[1] To overcome this major drawback, we have previously conjugated the anticancer drug to squalene, a natural and biocompatible lipid, and it was found that the resulting bioconjugate was able to self-assemble into nanoparticles in water. This nanomedicine displayed increased anticancer efficiency and decreased cardiotoxicity compared to free doxorubicin. This could be attributed to the elongated shape of Squalenoyl-doxorubicin (SQ-Dox) nanoparticles.[2] Long flexible cylindrical micelles, generally referred to as worm-like micelles or filomicelles, have been first used for therapeutic purposes by Discher *et al.* in the middle 2000s.[3,4] Interestingly, cylindrical paclitaxel-loaded polyethylene glycol-polycaprolactone nanoparticles were observed to exhibit an extended circulation time in mouse bloodstream compared to analogous spherical particles and a higher accumulation in xenograft tumors. Since then, increasing attention has been paid to the role of nanocarrier's shape for drug delivery. It has been revealed that beyond sustaining a long circulation time, elongated shape may favor margination (preferential migration of some nanoparticles close to the vessel wall in the bloodstream), allowing an improved delivery to target tissues *via* the enhanced permeation and retention effect.[5] In addition, the nanoparticle rigidity may also impact the tumor accumulation: soft nanocarriers accumulate more in tumor tissues than the stiffer ones.[6,7] All these findings help to consider worm-like nanoparticles as promising nanomedicines with a high degree of adjustability.

Received: July 5, 2019
Accepted: October 11, 2019
Published: October 11, 2019

DOI: 10.1021/acsnano.9b05303
ACS Nano 2019, 13, 12870−12879

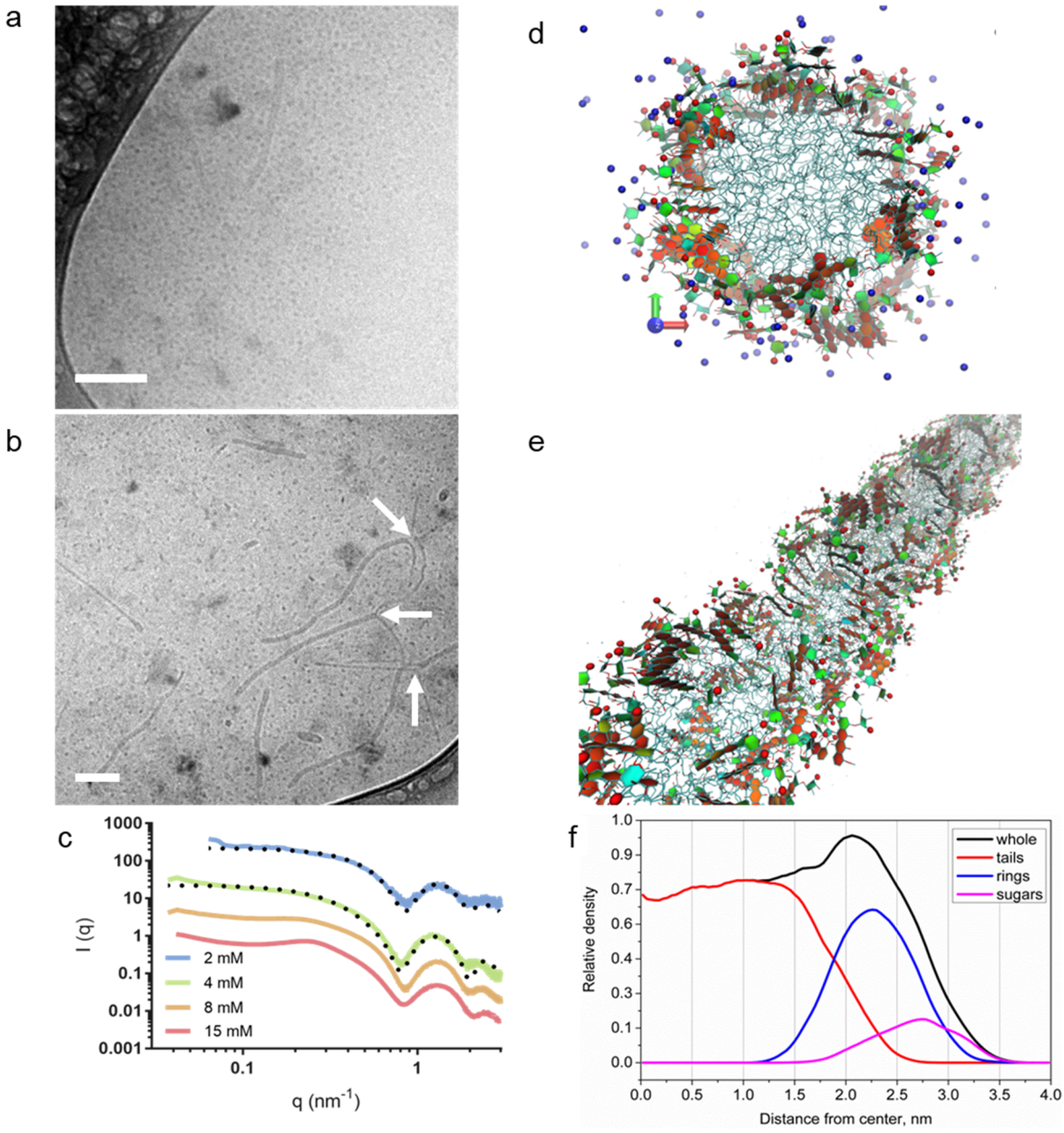

Figure 1. Structural characterization of SQ-Dox nanoparticles (a, b). Cryo-TEM micrographs of SQ-Dox nanoparticles suspensions prepared at (a) 2 mM (scale bar, 50 nm) and (b) 4 mM of SQ-Dox in water. The arrows indicate the interaction sites between SQ-Dox thin cylinders (scale bar, 100 nm). (c) Small-angle X-ray scattering pattern of SQ-Dox nanoparticles in water. The plain lines represent experimental data, and the dotted lines are the corresponding fits. Curves are shifted along the *y*-axis for clarity. (d, e) Snapshots of a cylindrical nanoparticle. SQ tails are shown as sticks. Aromatic rings are filled with red and orange, while nonaromatic rings are green and cyan. Positively charged NH_3^+ groups are shown as red spheres. Na^+ ions are blue spheres. Water is not shown for clarity. (d) Front view. (e) Perspective view. (f) Radial density distribution (in dimensionless units) of the SQ chains and Dox heads in the cylindrical nanoparticle with Cl^- counterions.

As the majority of the efforts has been put on polymer worm-like nanoparticles in recent years,[8−10] SQ-Dox is currently a simple nonpolymeric nanomedicine forming elongated nanostructures with confirmed therapeutic efficacy. But the mechanism allowing the formation of these worm-like structures remained completely unknown, and this has been extensively investigated in the current study. SQ-Dox molecule combines amphiphilic lipid-like properties with the net positive charge and strong stacking propensity of the Dox moiety, which makes it, indeed, an interesting model object for elucidating the role of these properties in the controllable formation of elongated nanoparticles. The experimental and computational techniques were used complementary for all the steps of the nanoparticle formation, which allowed studying this process in detail. Herein, we show that stacking interactions of Dox moieties play a major role in the self-assembling of elongated nanoparticles and their aggregation and reshaping in solution. The role of the added anion concentration and valency is also highlighted, as a simple way to modulate the nanoparticle shape and rigidity. This could bring interesting opportunities to the drug delivery field by designing nanomedicines with controlled shape and structure.

DOI: 10.1021/acsnano.9b05303
ACS Nano 2019, 13, 12870−12879

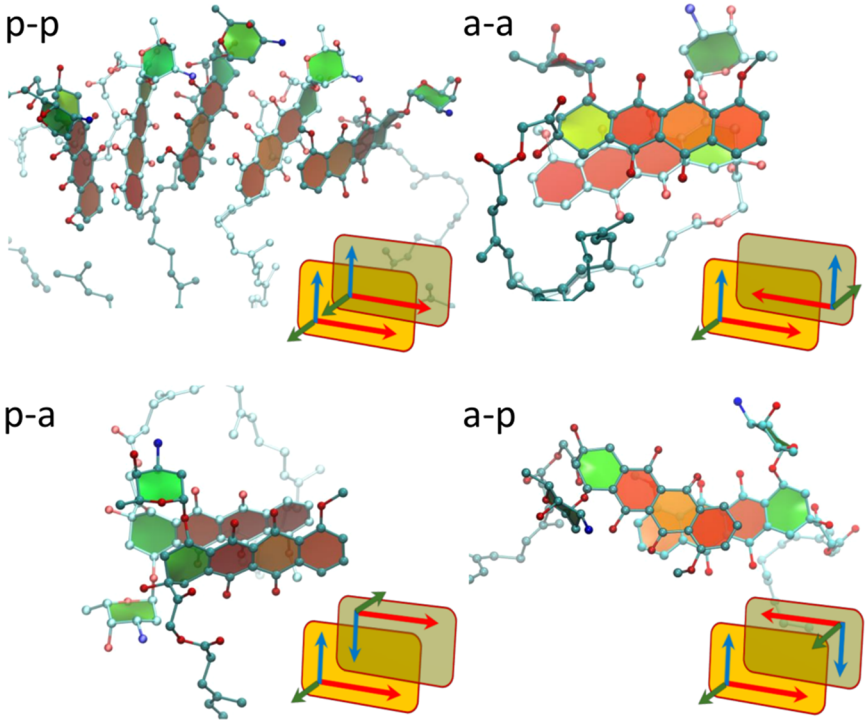

Figure 2. Different types of stacked aggregates observed in MD simulations. Each panel shows a simulation snapshot with stacked SQ-Dox molecules in corresponding configuration and a scheme of the aggregate. The red, blue, and green arrows correspond to long, short, and normal axes of the Dox rings respectively (see Supporting Information for details). Schemes are not aligned with the molecules on snapshots and correspond to them up to a three-dimensional rotation. On the first panel, the fan-like aggregate of five stacked molecules in p−p orientation is shown. Other panels show aggregates of two molecules.

RESULTS AND DISCUSSION

Structure of SQ-Dox Nanoparticles. SQ-Dox nanoparticles were prepared by nanoprecipitation of a THF solution of SQ-Dox hydrochloride in water, as previously described.[2] Clear red suspension of nanoparticles formed with a ζ-potential of ∼ +56 mV, arising from the positively charged ammonium group on the daunosamine sugar moiety of Dox. Cryo-TEM pictures of the 2 mM SQ-Dox nanoparticles suspension revealed the presence of small quasi-spherical nanoparticles with ∼5−6 nm diameter and only few long cylinders (Figure 1a). When increasing the concentration of SQ-Dox from 2 mM to 4 mM, cryo-TEM observations revealed the coexistence of short nanoparticles and worm-like nanoparticles with lengths up to microns (Figures 1b and S1a). In addition, some flexible nanoparticles of diameter ∼5 nm seemed to assemble to form thicker ones of diameter ∼11.7 nm. Generally, it was observed that the number of long worm-like nanoparticles increased when raising the SQ-Dox concentration. To investigate the reversibility of nanoparticles elongation, 4 mM Sq-Dox nanoparticles were diluted to 20 μM prior to atomic force microscopy (AFM) imaging. The obtained pictures showed that even when diluted, long worm-like nanoparticles remained in the suspension (Figure S1b,c), which suggested that these elongated nanoparticles were stable upon dilution.

Figure 1c displays the small-angle X-ray scattering (SAXS) patterns of nanoparticle suspensions depending on SQ-Dox concentration. The SAXS pattern of SQ-Dox suspensions at 2 mM concentration was modeled by core−shell prolate ellipsoids. The obtained lengths for short and long semiaxes were 2.3 ± 0.1 nm and 3.4 ± 0.1 nm, respectively, and the shell thickness was 1.1 ± 0.1 nm, in good agreement with cryo-TEM findings (Figure 1a). The SAXS patterns of more concentrated suspensions (4−15 mM) were characteristic of cylindrical nanoparticles, as shown by the q^{-1} dependence of the scattered intensity $I(q)$ at intermediate scattering vectors q ($q = 4\pi \sin \theta/\lambda$, where 2θ is the scattering angle and λ the X-ray wavelength).[11] In the high q region, short length scales were probed, and the curves reflected the structure of the nanoparticle cross-section. The intermediate and high q regions of the curves could be well described with a model of core−shell cylindrical aggregate, the core and the shell corresponding to the hydrophobic SQ chains and the hydrophilic Dox polar heads, respectively (Figure 1d,e). Fitting of the SAXS curve resulted in a core radius of 2.2 ± 0.1 nm, matching the length of stretched SQ chains, and a shell thickness of 1.1 ± 0.1 nm. The fitting method is described in Supporting Information.

The low q region contained information on the length and flexibility of the nanoparticles. Those features are expected to depend on the bioconjugate concentration. When the concentration increased, elongated nanoparticles tended to grow in order to minimize the excess of the free energy in the system by reducing the number of end-caps. Simultaneously, the rate of growth may be decreased by the electrostatic repulsions between charges along the nanoparticle body, favoring shorter nanoparticles.[12,13] The SAXS pattern of the 4 mM suspension could be fitted by ∼18 nm-long cylinders. The increase in $I(q)$ at lowest q values suggested the coexistence of these majority nanoparticles with long nanoassemblies. Upon aging, short cylinders evolved toward long worm-like nanoparticles with $2l_p \sim 40$ nm, as shown by the SAXS curve recorded after 18 days (Figure S2), where l_p is the persistence length, defined as the shortest scale over which a

DOI: 10.1021/acsnano.9b05303
ACS Nano 2019, 13, 12870−12879

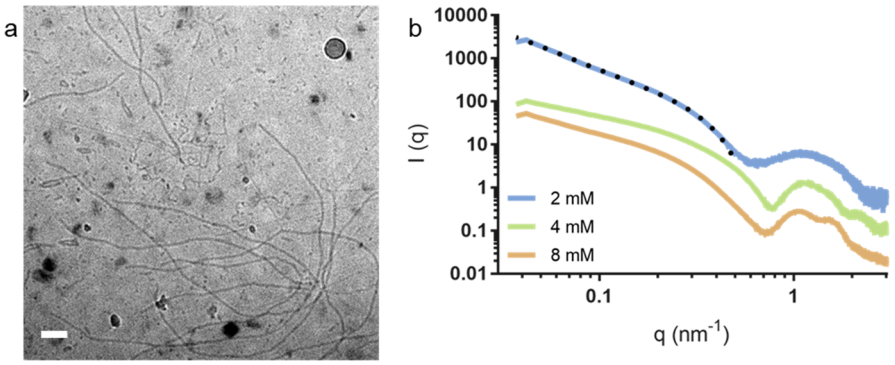

Figure 3. Morphological evolution of SQ-Dox nanoparticles. (a) Cryo-TEM micrograph of a suspension of nanoparticles prepared at a concentration of 2 mM in H_2O with addition of 2 mM NaCl (scale bar, 100 nm). (b) Influence of salt addition on nanoparticles SAXS patterns. The SQ-Dox nanoparticles are prepared at concentrations ranging from 2 mM to 8 mM, and NaCl is added using a molar ratio SQ-Dox:NaCl 1:1. The dotted line corresponds to the fit of the 2 mM curve. The curves have been shifted along the *y*-axis for clarity.

nanoparticle can be considered as a rigid rod.[12,13] Short l_p allows more flexibility, while cylinders rigidity increases for higher persistence lengths. For SQ-Dox concentration above 4 mM, the flattening in X-ray scattering intensity at low q and the broad maximum at about 0.24 nm^{-1}, indicative of a structure factor, emphasized the existence of repulsive interactions between nanoparticles, with an average distance between cylinders $d \sim 26$ nm. The interactions between nanoparticles depend on the effective volume fraction and dimensions of the nanoparticles. Due to the presence of charges, the diameter $2R$ of the nanoparticles was increased to the effective value $2R + 2\lambda_D$, where λ_D is the Debye screening length accounting for the extent of the electrostatic repulsion. The volume of a nanoparticle of length l was increased to the effective volume $\pi l(R + \lambda_D)^2$ (Table S1). Of note, the existence of interactions between nanoparticles is a major obstacle to determine their actual persistence length because the scattering in the low q region is affected by both the length of the nanoparticles and their interactions. Scattering in the intermediate q region provided the lower limit of the actual persistent (or nanoparticle) length (~13−20 nm).

The coexistence of rather short and long worm-like nanoparticles was further supported by the ultracentrifugation of the 8 mM SQ-Dox suspension. The supernatant SAXS pattern could be modeled by rod-like particles with length of ~20 nm, while the pellet pattern showed longer aggregated nanoparticles (Figure S3).

The radial density distribution obtained from molecular dynamics (MD) calculations was in excellent agreement with these findings (Figure 1f). During the simulations (Figure 1d,e), spontaneous formation of cylindrical nanoparticles could be observed from initial unstructured SQ-Dox aggregates on the time scale of hundreds of nanoseconds (Figure S4).

Of note, the formation of cylindrical aggregates is specific to SQ-Dox and contrasts with the shape of other squalene-based nanoparticles.[14−17] We assume that it originates from Dox stacking. Indeed, Dox is known to self-assemble in aqueous solution to form dimers, in parallel or antiparallel orientation, oligomers, or fibers, depending on the concentration, the pH of the solution, and the presence of added salts.[18−23] The absorbance and fluorescence spectra of SQ-Dox in water confirmed the stacking of Dox moieties in nanoparticles for concentration above 5 μM (Figure S5).

In simulated SQ-Dox aggregates, the stacks started forming within hundreds of picoseconds and persisted on the time scales of hundreds of nanoseconds up to the end of the simulations. Four distinct types of stacks were observed, differing in the relative orientation of the Dox rings (Figure 2). We classified the stacks by the relative orientation of the long axes and normal of Dox ring systems (see Supporting Information for detailed description). The p−p stacks were the most abundant and tended to form extended fan-like structures, including up to six molecules with long axes slightly inclined to each other. Three subpopulations of p−p pairs, which differed in the inclination angle α and the distance d: p−p_1 ($d \sim 0.55$ nm, $\alpha \sim 20°$): p−p_2 ($d \sim 0.45$ nm, $\alpha \sim 40°$); p−p_3 ($d \sim 0.45$ nm, $\alpha \sim 60°$), coexisted in cylindrical nanoparticles (Figure S6a). The free energy barrier of disrupting the p−p_1 stacking interaction in cylindrical micelles was estimated in MD simulations as ~30 kJ mol^{-1} (Figure S7). This indicated strong interaction with characteristic lifetime of minutes. The a−a and p−a stacks were also observed, while a−p stacks were very rare (Figure S6b). Despite numerous subpopulations of stacked pairs, the orientation of Dox heads relative to the radius of cylinders was rather homogeneous and formed a single dominant population (Figure S6c). However, the relative abundances of the different types of stacks could not be quantified since the molecule stacking was correlated with the nanoparticle density, given in arbitrary units.

To confirm the preferential assembling of SQ-Dox into cylindrical aggregates, the packing parameter p has been evaluated through Langmuir−Blodgett experiments. A molecular area of 53 Å^2 was deduced from the SQ-Dox monolayer compression isotherm (Figure S8a), leading to a p value of 0.51, clearly consistent with the formation of cylindrical nanoparticles.[24] The compressibility modulus K for the SQ-Dox monolayer exhibited a maximum value of 92 mN·m^{-1}, higher than the compressibility modulus maxima of squalenic acid and squalene-based cytidine derivatives, comprised in the 43−62 mN·m^{-1} range (Figure S8b).[25] This is likely a consequence of Dox stacking. Interestingly, this maximum was obtained for a large range of surface pressure, suggesting possible molecular reorganization in the monolayer.

Influence of Salt on SQ-Dox Nanoparticles Structure. The influence of adding NaCl to an already prepared SQ-Dox nanoparticle suspension in water was investigated, using a SQ-Dox:NaCl ratio of 1:1 mol:mol. Added salts are expected to screen the intramicellar repulsive interactions between charges, entailing the growth of aggregates.[12] Cryo-TEM pictures revealed that compared to SQ-Dox in pure water, the number

DOI: 10.1021/acsnano.9b05303
ACS Nano 2019, 13, 12870−12879

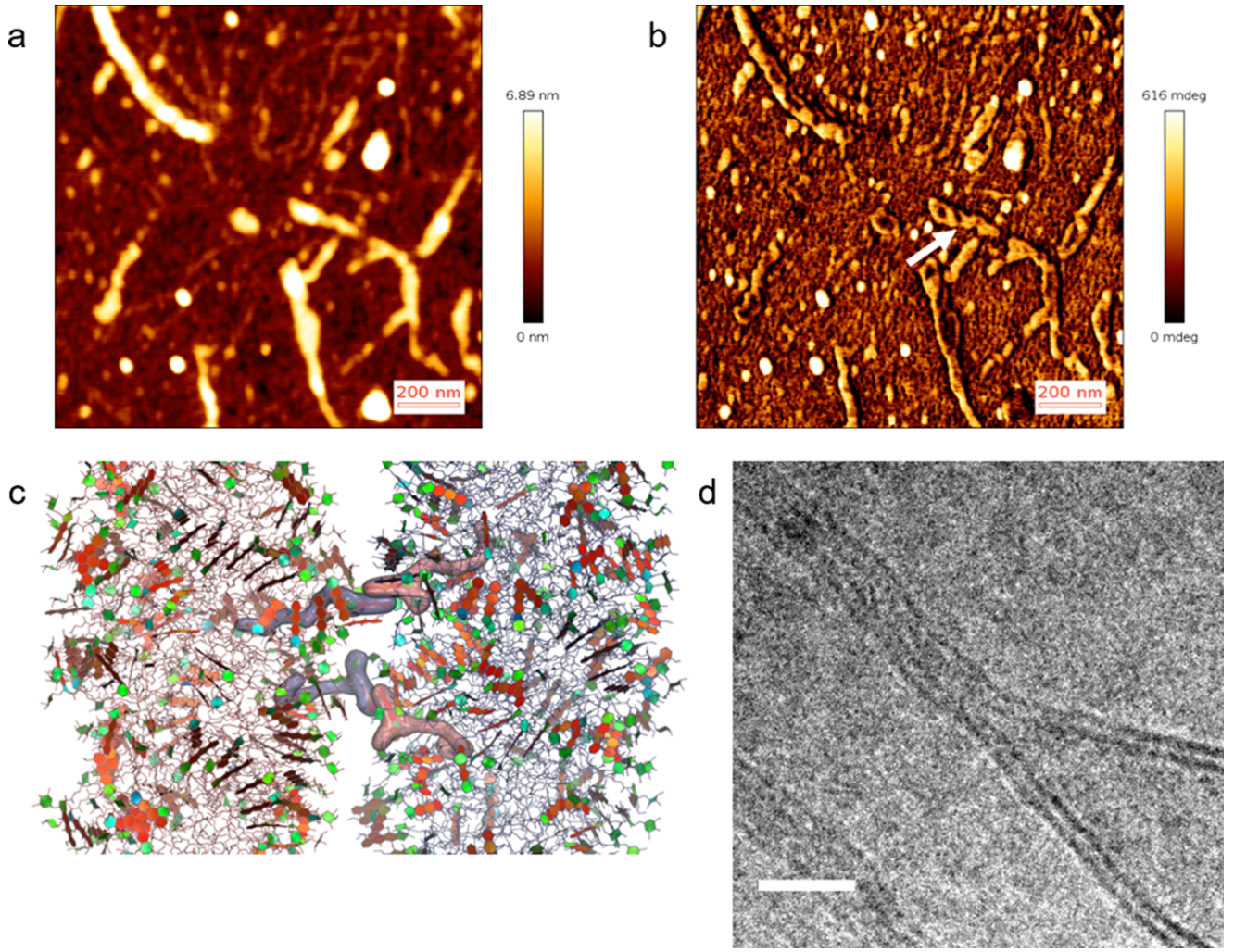

Figure 4. Mechanism of interaction between cylindrical nanoparticles with monovalent anions. (a, b) AFM pictures obtained in liquid medium of SQ-Dox nanoparticles (2 mM with 2 mM NaCl, scale bar, 200 nm). (a) Height image. (b) Phase image. (c) MD simulations showing intercylinders stacking interactions. Stacking pairs from different cylinders are highlighted by semitransparent surfaces. The colors are the same as in Figure 1. (d) Cryo-TEM pictures show the stacking of SQ-Dox nanoparticles (2 mM with 2 mM NaCl) to form multilayer structures (scale bar, 20 nm).

and the length of long worm-like nanoparticles increased after NaCl addition and the two previously described populations with diameters ∼5 nm and ∼11.7 nm were detected (Figure 3a).

The SAXS pattern of a 2 mM SQ-Dox nanosuspension in the presence of 2 mM NaCl revealed the formation of long worm-like nanoparticles (Figure 3b). The scattered intensity $I(q)$ showed a clear upturn in the low q region ($q \leq 0.25$ nm^{-1}) relative to the q^{-1} behavior typical of straight rods observed at intermediate q values. In the 0.05−0.5 nm^{-1} q-range, the curve could be fitted with the two models of long semiflexible chains without interactions developed by Kholodenko and Pedersen and Schurtenberger.[26,27] They yielded similar Kuhn lengths $2l_p \sim 30$ nm. For nanoparticles prepared at 4 mM and 8 mM, the repulsive interactions between the nanoparticles were screened upon addition of NaCl, as shown by the disappearance of the correlation peak at $q \sim 0.24$ nm^{-1} compared to nanoparticles in water (Figure 1d) and by the q^{-1} dependence of the scattered intensity extending at low q values (Figure 3b). The decrease of the Debye lengths λ_D also confirmed this screening process (Table S1). The SAXS pattern of the 4 mM suspension could be fitted with a model of 100 nm-long stiff cylinders. However, according to cryo-TEM pictures, this length could rather describe the persistence length. Taken together, the above results suggested an increase of nanoparticle flexibility with the addition of NaCl.

The screening of repulsive interactions between cylindrical aggregates may favor their side-by-side association, as suggested by the scattering curve in the high q region of the SQ-Dox nanoparticles at a concentration of 8 mM with NaCl at molar ratio 1:1 (Figure 3b). A factor structure, resulting from the close packing of some cylinders, was superimposed on the oscillation at high q, while the low-q part of the curve could be fitted, as above, with 100 nm-long rods, here displaying an ellipsoidal cross-section. The length of the short semi-axis and the ellipticity ratio were 3.8 nm and 2.2, respectively, consistent with the size of the thicker nanoparticles. The peaks at 0.94 nm^{-1} and 1.7 nm^{-1} corresponded to the first and second order of reflection arising from the stacking of cylinders with a mean distance between their axes of ∼6.7 nm, consistent with their diameter.

Additional insights into the structure of the SQ-Dox nanoparticles were provided by AFM imaging. It has been

DOI: 10.1021/acsnano.9b05303
ACS Nano 2019, 13, 12870−12879

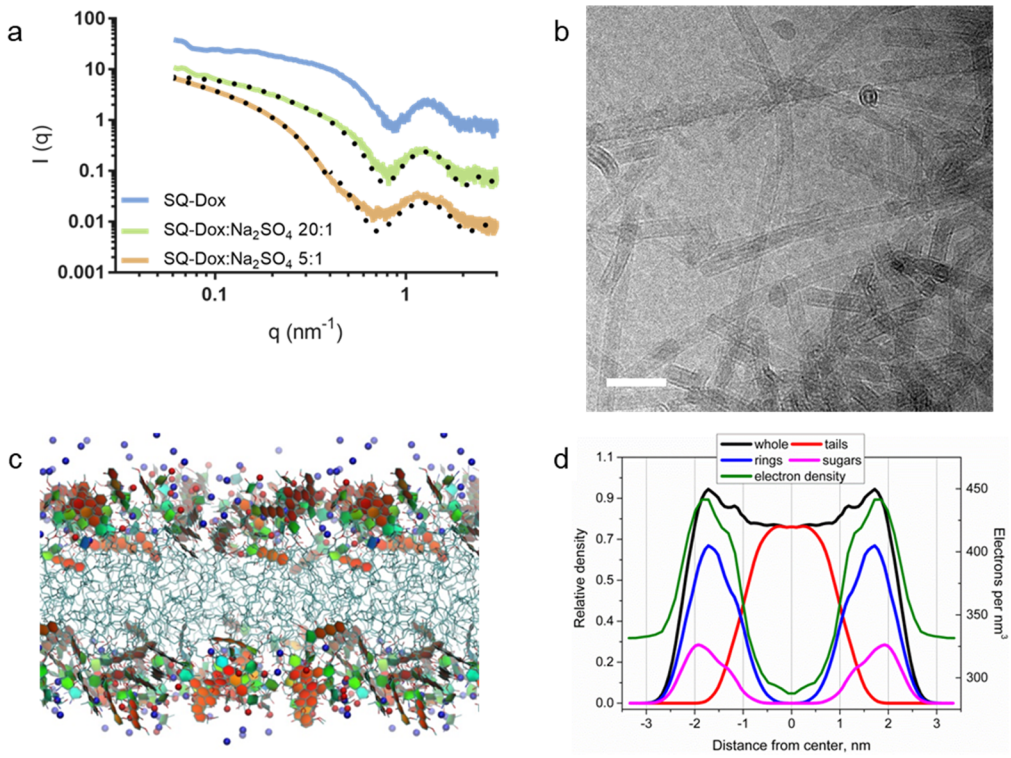

Figure 5. Morphology of SQ-Dox nanoparticles in the presence of divalent anions. (a) SAXS patterns of SQ-Dox nanoparticles in the presence of Na_2SO_4. The SQ-Dox nanoparticles are prepared at 2 mM, and Na_2SO_4 is added at 0.01 mM (molar ratio 20:1) or 0.04 mM (molar ratio 5:1). The dotted lines correspond to the fits of the experimental curves. The curves have been shifted along the *y*-axis for clarity. (b) Cryo-TEM micrograph of a suspension of SQ-Dox nanoparticles at a concentration of 2 mM with addition of 0.04 mM Na_2SO_4 (Scale bar, 50 nm). (c) Snapshot of equilibrated SQ-Dox bilayer. Squalene tails are shown as sticks. Aromatic rings are filled with red and orange while non-aromatic rings with green and cyan. Positively charged NH_3^+ groups are shown as red spheres. Na^+ ions are blue. Water is not shown for clarity. (d) Density profiles for equilibrated SQ-Dox bilayer including electron density profile.

observed that the AFM height image of the SQ-Dox samples displayed a mixture of spheres and long cylinders affected in two ways: (i) by the attractive interactions between the positively charged nanoparticles and the silicon surface that tended to flatten the nanoparticles and (ii) by the convolution between the AFM tip and nanoparticles lateral dimensions (Figure 4a). The AFM phase image suggested that thin cylinders formed helical bundles during their aggregation into thick cylinders (see arrow in Figure 4b). The MD simulations of interacting worm-like nanoparticles also highlighted the formation of twisted aggregates, which could also form helical bundles on larger scales (Figure S9).

MD simulations also revealed the existence of intercylinder stacking interactions involving a−a and a−p stacking pairs. Although the formation of such "bridges" was rare (only two pairs were formed during the simulation time of 300 ns), they were able to keep the cylinders together once formed. This allowed us to hypothesize a "zipper-like" mechanism of interaction between the cylinders (Figure 4c). Once several intercylinder stacks formed, they would keep the cylinders at close distance for a sufficiently long time to facilitate the formation of even more stacks. The formation of "zipped" cylinders was also clearly observed by cryo-TEM (Figure 4d).

Influence of the Nature of the Salt on the Structure of the SQ-Dox Nanoparticles. In order to investigate the impact of the nature of the salt on the supramolecular assembly of SQ-Dox, Na_2SO_4 was added to a 2 mM water suspension of nanoparticles, with addition of 0.01 to 1 mM Na_2SO_4 (SQ-Dox:Na_2SO_4 ratios 20:1 to 2:1 mol:mol, respectively). Using 0.01 mM Na_2SO_4, long core−shell cylinders were observed as the main population (Figure 5a), while with higher Na_2SO_4 concentrations, the divalent anions allowed the formation of wider (d ∼14.3 nm, Figures 5b and S10a), shorter, and more rigid cylindrical nanoparticles compared to monovalent anions (*i.e.*, NaCl). The SAXS curve at low q could be modeled by cylinders with a log normal distribution of radii around 7 nm, in agreement with the diameters measured in cryo-TEM experiment (Figure 5a). Both Cryo-TEM images and SAXS pattern suggested the formation of nanotubes consisting of an aqueous core surrounded by a SQ-Dox bilayer. Some images also suggested the existence of nanoassemblies comprising a SQ-Dox cylindrical core surrounded by a bilayer shell (Figure S10b).

The possible formation of stable bilayers with an average thickness of ∼4 nm was supported by MD simulation (Figures 5c,d and S11a,b). Experimentally, the rod-to-bilayer transition was expected to arise from both the screening of charges and the ability of divalent anions to form long-lived bridges between charged Dox moieties. The distributions of the distances between N atoms of the sugar moieties in stacked Dox pairs were computed for Cl^- and SO_4^{2-} ions, demonstrating that these distances were significantly shorter in the presence of SO_4^{2-} ions (Figure S11c). The decrease in electrostatic repulsion and salt bridges between nearest-neighbor amine groups led to a denser packing of SQ-Dox molecules, along with an increase in the packing parameter and a lower curvature of the nanoparticles. The bilayers thus formed were flexible enough to bend into cylinders.

DOI: 10.1021/acsnano.9b05303
ACS Nano 2019, 13, 12870−12879

Interestingly, some cryo-TEM images suggested the wrapping of a bilayer around a SQ-Dox cylinder (Figure S10b). The formation mechanism could rely on the adsorption of SQ-Dox monomers at the surface of cylindrical nanoparticles through the formation of SO_4^{2-} bridges. The bilayer could then be generated by the addition of another layer of monomers to avoid unfavorable interaction of SQ chains with water. Tubes of 16−17 nm diameter, consisting in a SQ-Dox bilayer separated from the cylindrical core by a thin layer of water, were constructed in MD simulations (Figure S10c,d). The density map of Dox headgroups in the cross-section, symmetrized radially around the axis of the tube, exhibited three distinct rings corresponding to the layers of Dox moieties located at distances of ∼2.2 nm, ∼4.1 nm, and ∼7.5 nm from the center. Those values are in good agreement with cryo-TEM findings (Figure S10b,e).

Discussion. So far, two main delivery strategies have been employed to reduce the toxicity and improve the efficacy of Dox: (i) the encapsulation of Dox into nanocarriers, usually liposomes or polymeric carriers and (ii) the design of prodrugs activated by an enzyme overexpressed in the tumor microenvironment or by an acidic pH.[28] SQ-Dox is a simple lipid-like molecule which combines the properties of a prodrug and the ability to self-assemble as elongated nanoparticles in water to ensure enhanced pharmacological activity, making it appealing for clinical perspective. The structure of the nanoparticles results from the interplay between hydrophobic interactions of squalene chains and stacking and electrostatic interactions of Dox head groups. Absorbance and fluorescence experiments revealed the stacking of Dox heads, whose MD simulations gave a more quantitative description. Stacking interactions of Dox heads not only lead to the formation of cylindrical nanoparticles instead of spherical, but such interactions also result in an impressive heterogeneity of nanoparticles surfaces, which contain four distinct topologies of stacks subdivided further into a number of subpopulations. The minor population of antiparallel stacks is especially important because of its ability to "zip" cylindrical nanoparticles together, leading to the formation of bundles and other complex aggregates, especially in the presence of salts. The charge of the Dox headgroups adds, indeed, another dimension for adjusting and controlling the nanoparticles structure. Addition of monovalent salts resulted in the elongation of cylindrical nanoparticles, which could be beneficial for prolonging the blood circulation time and avoiding the capture by the macrophages of the reticuloendothelial system. But divalent anions provided another mechanism of assembly by means of salt bridges, triggering a dramatic transition from individual cylindrical nanoparticles to bilayer tubes in solutions in the late stages of their evolution. Suggested sequence of events during the evolution of SQ-Dox nanoparticles in different salt solutions is shown in Figure 6.

It has been reported in the literature that self-assembled nucleolipids may exhibit a variety of morphologies, including worm-like micelles, that depend on both the nucleosidic headgroups and the lipid chains.[29−31] The phase behavior of SQ-Dox demonstrates that polar heads other than those derived from a nucleobase can guide the self-assembly of lipid-based bioconjugates into complex structures such as rod-like nanoparticles. Moreover, previous experiments on squalene-based nucleolipids have shown that squalene chains could fit into various structures such as inverse hexagonal phases or bilayers forming liposomes, lamellar phases, inverse bicontinuous cubic phases, or sponge phases.[25] Coupling squalene with other polar drug molecules capable of $\pi-\pi$ interactions (*e.g.*, camptothecin and derivatives, ciprofloxacin, *etc.*)[32,33] could therefore be envisioned to broaden the approach and to design nonspherical drug-delivery systems. In addition, the excellent agreement between experimental results and MD simulations suggests that computational techniques could be used to screen bioconjugates prone to self-assemble as elongated nanoparticles.

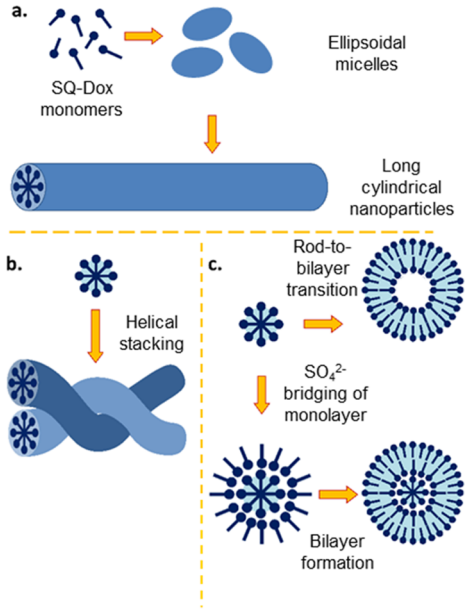

Figure 6. Schematic representation of the mechanisms of SQ-Dox assembly into elongated nanoparticles. (a) Early stages of assembly − spontaneous formation of short cylindrical micelles and their elongation. (b) Late stages of assembly with monovalent anions. (c) Late stages of assembly with divalent anions. Dox headgroups are shown as filled circles and squalene tails as rods. In (b) and (c), the hydrophobic areas are cyan, while white areas are assumed to be filled with water.

Altogether, these results raise another concern about the preservation of the nanodrugs properties after administration in patient body. For example, the shape of nanoparticles influences their circulation in the bloodstream, while their size drives the filtration processes. Adjusting shape and surface charge may also help to avoid capture by the macrophages and the reticuloendothelial system.[34] We demonstrated here that those parameters may be radically modified by addition of species as simple as basic ions, naturally present in the blood. The investigation of this feature seems particularly relevant for the development of nanoparticles specifically engineered to reach particular targets.

CONCLUSION

We demonstrated here that the shape, size, and surface properties of SQ-Dox nanoparticles could easily be modulated in broad ranges by varying the bioconjugate concentration, the ionic strength, and the nature of the anion. But the present study also suggests that the nanoparticles in the test tube and in the body may not be the same since their structure may dramatically vary according to the local *in vivo* environment, and this may have some clinical implications. Nevertheless, SQ-Dox may serve as a model for creating lipid-like self-

DOI: 10.1021/acsnano.9b05303
ACS Nano 2019, 13, 12870−12879

assembling molecules with stacking and cross-linking behavior tuned for particular medical applications.

MATERIALS AND METHODS

Materials. All solvents were purchased from Carlo-Erba (Val-de-Reuil, France), and doxorubicin and daunorubicin hydrochloride were purchased from APAC Pharmaceutical LLC (Ellicott City, MD). Squalene, doxorubicin hydrochloride, sodium acetate, sodium chloride, and sodium sulfate were purchased from Sigma-Aldrich Chemical Co. (St. Quentin Fallavier, France), and TLC plates and silica gels for chromatography were purchased from Merck (Darmstadt, Germany).

Formulation and Characterization of SQ-Dox Nanoparticles. SQ-Dox was synthesized as described in Supporting Information. SQ-Dox nanoparticles were prepared according to the nanoprecipitation process, adapted from Maksimenko *et al.*[2] Practically, SQ-Dox (2 mg) was solubilized into 500 μL of THF and added dropwise in 1 mL of H_2O under stirring (500 rpm) using a syringe pump with a flow rate of 130 μL min. THF was then removed by evaporation at 20 °C under vacuum to obtain a suspension of SQ-Dox nanoparticles in water.

To study the influence of added salts, concentrated solutions were added to already prepared SQ-Dox nanoparticle suspensions. NaCl solutions were prepared at concentrations ranging from 200 to 800 mM. 2 μL of salt solution of appropriate concentration was added to 200 μL of SQ-Dox nanoparticles in water prepared at concentrations ranging from 2 mM to 8 mM, to reach a final SQ-Dox:NaCl molar ratio of 1:1. Na_2SO_4 solutions were prepared at concentrations ranging from 10 to 100 mM. 2 μL of salt solution of appropriate concentration was added to 200 μL of 2 mM SQ-Dox nanoparticles in water to reach a final SQ-Dox:Na_2SO_4 molar ratio ranging from 20:1 to 2:1.

The ζ-potential was measured at 25 °C after 1:10 dilution of SQ-Dox nanoparticles in 1 mM NaCl solution using a Zetasizer Nano ZS (Malvern Panalyticals).

Cryo-Transmission Electron Microscopy. 5 μL of SQ-Dox nanoparticles at different concentrations (2 mM, 4 mM or 8 mM) in pure water or in the presence of salts (NaCl or Na_2SO_4 at molar ratios SQ-Dox:NaCl 1:1 or SQ-Dox:Na_2SO_4 20:1 to 2:1) were deposited onto a Lacey Formvar/carbon 300 mesh copper grid (Ted Pella). The excess was manually blotted with a filter paper, and the residual thin film was immediately frozen by plunging into liquid ethane cooled down at liquid nitrogen temperature using a Leica EM-CPC cryo-plunger. Observation was performed using a JEOL 2100HC microscope (JEOL Europe) or a JEOL 2200FS field emission microscope (JEOL USA) operating under an acceleration voltage of 200 kV in zero-loss mode (slit was 20 eV). High-magnification images (2k × 2k pixels) were recorded by a CCD camera (Gatan Inc.) using Digital Micrograph software.

Atomic Force Microscopy. SQ-Dox nanoparticles samples (2 mM SQ-Dox with NaCl 2 mM and 4 mM SQ-Dox in water) were diluted to 20 μM in water. 1 mL of this nanoparticle suspension was then deposited during 2 h onto a hydrophilic silicon surface previously treated with acidic piranha solution. AFM experiments were performed using the Nanowizard 3 Ultra Speed (JPK Instruments), installed on an air-buffered table coupled to a dynamic antivibration device, and enclosed in an acoustic box. Imaging of the surface morphology was performed in air in AC mode with gold-coated silicon cantilever MLCT of 0.6 ± 0.1 N.m^{-1} spring constant, 170 ± 5 kHz resonance frequency, and 10 nm nominal radius of curvature (Bruker). The pyramid-shaped tips had a radius of curvature <20 nm. A free amplitude oscillation of 15 nm was chosen allowing the best resolution of the imaged surface. Set points ranging between 75% and 85% of the free amplitude were used. Images were taken at scan rate of 1 Hz. Image processing (flatten, plane fit, edge, and hole detection) was performed with the JPK Data Processing software (JPK Instruments). At least three different areas of each sample were scanned and typical images were presented.

Small Angle X-ray Scattering. SAXS experiments were performed on the SWING beamline at SOLEIL and on the BM29 beamline at ESRF. For measurements on the SWING beamline, samples were loaded into quartz capillaries (1.5 mm diameter). The scattering intensity $I(q)$ was reported as a function of the scattering vector $q = 4\pi \sin\theta/\lambda$, where 2θ is the scattering angle and λ the X-ray wavelength. Data were recorded at 12 keV in the scattering vector q-range $0.04 < q < 4$ nm^{-1}, using a bidimensional Aviex detector. For each sample, 10 frames of 0.150 s were recorded at 20 °C and averaged. Water scattering was subtracted from the sample scattering. The beamline software Foxtrot was used for data collection and processing. On the BM29 beamline, samples were injected *via* an automated sample changer into a quartz capillary (1.8 mm internal diameter) and streamed at a constant flow rate through the capillary during beam exposure to avoid possible degradation under X-ray irradiation.[35] Data were recorded at 12.5 keV in the scattering vector q-range $0.04 < q < 5$ nm^{-1}, using a Pilatus 1 M detector. For each sample 12 frames of 0.3 s were averaged, and water scattering was measured before and after each sample.[36] The dedicated beamline software BsxCuBe was used for data collection, and data processing was carried out using EDNA software.[37] For all of the samples, the scattering intensity was normalized with respect to the incident beam intensity, acquisition time, and sample transmission. Structural information was retrieved from the SAXS patterns using the SASfit program.[38]

Molecular Dynamics Force Field. The topology of SQ-Dox was used from our previous study.[39] Initial topology of SQ-Dox was generated by an Acpype topology generator.[40] The structure was optimized in Gaussian 09[41] at the B3LYP/6-31++G(d) level of theory. The ESP partial charges were computed and added to initial topology. The charges of topologically equivalent atoms were averaged. The charges of squalene moiety were set to zero except the linker between Dox and SQ. The atom types of SQ tails were adjusted to match lipids force field.

Construction of Prearranged Cylindrical Aggregates. Cylindrical aggregates were also constructed from the prearrangement of SQ-Dox molecules in preferred orientation. This allowed a much simpler simulation setup, which could be easily used to generate several initial structures for independent simulations. 100 SQ-Dox molecules were arranged into 10 disks with the molecules in each disk oriented radially around the z-axis with Dox moiety facing outside. The system was solvated with ∼13,000 water molecules and either 100 Cl^- or 100 SO_4^{2-} and 50 Na^+ counterions in such a way that the solvent did not penetrate into the region of the SQ tails. The system was equilibrated for 300 ns without any restraints.

Simulations of SQ-Dox Bilayers. In order to simulate the bilayer phase of SQ-Dox, the molecules were arranged into the monolayer at 7 × 7 grid in x,y plane with Dox moieties facing upward. The second inverted monolayer was added, and the system was solvated with ∼5,000 water molecules and the corresponding number of Cl^- counterions. No water molecules were placed into the region of SQ tails. The system was equilibrated for 300 ns without restraints. The area per molecule was used to monitor equilibration.

ASSOCIATED CONTENT

Supporting Information

The Supporting Information is available free of charge on the ACS Publications website at DOI: 10.1021/acsnano.9b05303.

Additional AFM pictures, cryo-TEM pictures, and SAXS patterns of SQ-Dox nanoparticles, spectroscopic analysis of Dox stacking properties, SQ-Dox monolayer characterization, simulation of the stacking pairs properties and repartition in SQ-Dox nanoparticles, Debye lengths calculations, SQ-Dox synthesis, and detailed associated methods (PDF)

DOI: 10.1021/acsnano.9b05303
ACS Nano 2019, 13, 12870−12879

AUTHOR INFORMATION

Corresponding Author

*E-mail: patrick.couvreur@u-psud.fr.

ORCID

Julie Mougin: 0000-0002-2118-860X
Semen O. Yesylevskyy: 0000-0002-6748-8931
Claudie Bourgaux: 0000-0001-7642-887X
David Chapron: 0000-0002-0944-288X
Franco Dosio: 0000-0003-1128-9922
Barbara Stella: 0000-0001-8266-6604
Patrick Couvreur: 0000-0001-7961-5443

Author Contributions

P.C. designed the research. B.S. and F.D. performed the chemical synthesis of SQ-Dox. J.M. performed the preparation of nanoparticles, the cryo-TEM observations, and the Langmuir−Blodgett and spectroscopic experiments. C.B. performed the SAXS experiments, analyzed the data, and helped calculate the packing parameter. D.C. helped to perform and to interpret the Langmuir−Blodgett experiments. J.-P.M. performed the AFM studies. S.Y. and C.R. performed and analyzed the molecular dynamics simulations. J.M., S.Y., and C.R. wrote the paper. All authors discussed the results and commented on the manuscript.

Funding

C.R. and S.Y. were supported by the European Union's Horizon 2020 research and innovation program under the H2020 Marie Sklodowska-Curie grant agreement nos. 690853 and 796245, respectively, and the NATO grant SPS-G5291.

Notes

The authors declare the following competing financial interest(s): P. Couvreur is the founder of the start-up company Squal Pharma.

ACKNOWLEDGMENTS

The authors thank ESRF and SOLEIL synchrotron facilities for the beamlines access and Gabriele Giachin (ESRF) and Javier Perez (SOLEIL) for their help with experiments. We also thank Ghislaine Frébourg (IFR 83 Biologie Intégrative, Paris, France), FRM 2006, SESAME 2005, and CNRS-ISB for providing access to JEOL 2100HC TEM, and Dr. Sylvain Trépout (Institut Curie, Orsay, France) and PICT-Ibisa for the experiments using JEOL 2200FS TEM. The Centre de calcul regional Romeo and the Mésocentre de calcul de Franche-Comté are deeply acknowledged for providing computational resources for this work.

REFERENCES

(1) Lefrak, E. A.; Piha, J.; Rosenheim, S.; Gottlieb, J. A. A Clinicopathologic Analysis of Adriamycin Cardiotoxicity. *Cancer* **1973**, *32*, 302−314.

(2) Maksimenko, A.; Dosio, F.; Mougin, J.; Ferrero, A.; Wack, S.; Reddy, L. H.; Weyn, A.-A.; Lepeltier, E.; Bourgaux, C.; Stella, B.; Cattel, L.; Couvreur, P. A Unique Squalenoylated and Nonpegylated Doxorubicin Nanomedicine with Systemic Long-Circulating Properties and Anticancer Activity. *Proc. Natl. Acad. Sci. U. S. A.* **2014**, *111*, E217−E226.

(3) Geng, Y.; Dalhaimer, P.; Cai, S.; Tsai, R.; Tewari, M.; Minko, T.; Discher, D. E. Shape Effects of Filaments *versus* Spherical Particles in Flow and Drug Delivery. *Nat. Nanotechnol.* **2007**, *2*, 249−255.

(4) Christian, D. A.; Cai, S.; Garbuzenko, O. B.; Harada, T.; Zajac, A. L.; Minko, T.; Discher, D. E. Flexible Filaments for *In Vivo* Imaging and Delivery: Persistent Circulation of Filomicelles Opens the Dosage Window for Sustained Tumor Shrinkage. *Mol. Pharmaceutics* **2009**, *6*, 1343−1352.

(5) Li, Y.; Lian, Y.; Zhang, L. T.; Aldousari, S. M.; Hedia, H. S.; Asiri, S. A.; Liu, W. K. Cell and Nanoparticle Transport in Tumour Microvasculature: The Role of Size, Shape and Surface Functionality of Nanoparticles. *Interface Focus* **2016**, *6*, 20150086.

(6) Champion, J. A.; Mitragotri, S. Shape Induced Inhibition of Phagocytosis of Polymer Particles. *Pharm. Res.* **2009**, *26*, 244−249.

(7) Sun, J.; Zhang, L.; Wang, J.; Feng, Q.; Liu, D.; Yin, Q.; Xu, D.; Wei, Y.; Ding, B.; Shi, X.; Jiang, X. Tunable Rigidity of (Polymeric Core)-(Lipid Shell) Nanoparticles for Regulated Cellular Uptake. *Adv. Mater.* **2015**, *27*, 1402−1407.

(8) Jelonek, K.; Li, S.; Wu, X.; Kasperczyk, J.; Marcinkowski, A. Self-Assembled Filomicelles Prepared from Polylactide/Poly(Ethylene Glycol) Block Copolymers for Anticancer Drug Delivery. *Int. J. Pharm.* **2015**, *485*, 357−364.

(9) Wan, X.; Min, Y.; Bludau, H.; Keith, A.; Sheiko, S. S.; Jordan, R.; Wang, A. Z.; Sokolsky-Papkov, M.; Kabanov, A. V. Drug Combination Synergy in Worm-Like Polymeric Micelles Improves Treatment Outcome for Small Cell and Non-Small Cell Lung Cancer. *ACS Nano* **2018**, *12*, 2426−2439.

(10) Nair, P. R.; Karthick, S.; Spinler, K. R.; Vakili, M. R.; Lavasanifar, A.; Discher, D. E. Filomicelles from Aromatic Diblock Copolymers Increase Paclitaxel-Induced Tumor Cell Death and Aneuploidy Compared with Aliphatic Copolymers. *Nanomedicine* **2016**, *11*, 1551−1569.

(11) Espinat, D. Principes Théoriques de La Diffusion Cohérente Statique. *Application des Techniques de Diffusion de la Lumière, des Rayons X et des Neutrons à l'Etude des Systèmes Colloïdaux*; Technip: Paris, 1992; pp 3−13.

(12) Dreiss, C. A. Wormlike Micelles: Where Do We Stand? Recent Developments, Linear Rheology and Scattering Techniques. *Soft Matter* **2007**, *3*, 956−970.

(13) Lequeux, F. Structure and Rheology of Wormlike Micelles. *Curr. Opin. Colloid Interface Sci.* **1996**, *1*, 341−344.

(14) Ralay-Ranaivo, B.; Desmaële, D.; Bianchini, E. P.; Lepeltier, E.; Bourgaux, C.; Borgel, D.; Pouget, T.; Tranchant, J. F.; Couvreur, P.; Gref, R. Novel Self Assembling Nanoparticles for the Oral Administration of Fondaparinux: Synthesis, Characterization and *In Vivo* Evaluation. *J. Controlled Release* **2014**, *194*, 323−331.

(15) Hillaireau, H.; Dereuddre-Bosquet, N.; Skanji, R.; Bekkara-Aounallah, F.; Caron, J.; Lepêtre, S.; Argote, S.; Bauduin, L.; Yousfi, R.; Rogez-Kreuz, C.; Desmaële, D.; Rousseau, B.; Gref, R.; Andrieux, K.; Clayette, P.; Couvreur, P. Anti-HIV Efficacy and Biodistribution of Nucleoside Reverse Transcriptase Inhibitors Delivered as Squalenoylated Prodrug Nanoassemblies. *Biomaterials* **2013**, *34*, 4831−4838.

(16) Gaudin, A.; Yemisci, M.; Eroglu, H.; Lepetre-Mouelhi, S.; Turkoglu, O. F.; Dönmez-Demir, B.; Caban, S.; Sargon, M. F.; Garcia-Argote, S.; Pieters, G.; Loreau, O.; Rousseau, B.; Tagit, O.; Hildebrandt, N.; Le Dantec, Y.; Mougin, J.; Valetti, S.; Chacun, H.; Nicolas, V.; Desmaële, D.; et al. Squalenoyl Adenosine Nanoparticles Provide Neuroprotection after Stroke and Spinal Cord Injury. *Nat. Nanotechnol.* **2014**, *9*, 1054−1062.

(17) Kotelevets, L.; Chastre, E.; Caron, J.; Mougin, J.; Bastian, G.; Pineau, A.; Walker, F.; Lehy, T.; Desmaële, D.; Couvreur, P. A Squalene-Based Nanomedicine for Oral Treatment of Colon Cancer. *Cancer Res.* **2017**, *77*, 2964−297.

(18) Menozzi, M.; Valentini, L.; Vannini, E.; Arcamone, F. Self-Association of Doxorubicin and Related Compounds in Aqueous Solution. *J. Pharm. Sci.* **1984**, *73*, 766−770.

(19) Agrawal, P.; Barthwal, S. K.; Barthwal, R. Studies on Self-Aggregation of Anthracycline Drugs by Restrained Molecular Dynamics Approach Using Nuclear Magnetic Resonance Spectroscopy Supported by Absorption, Fluorescence, Diffusion Ordered Spectroscopy and Mass Spectrometry. *Eur. J. Med. Chem.* **2009**, *44*, 1437−1451.

DOI: 10.1021/acsnano.9b05303
ACS Nano 2019, 13, 12870−12879

(20) Fülöp, Z.; Gref, R.; Loftsson, T. A Permeation Method for Detection of Self-Aggregation of Doxorubicin in Aqueous Environment. *Int. J. Pharm.* **2013**, *454*, 559−561.
(21) Li, X.; Hirsh, D. J.; Cabral-Lilly, D.; Zirkel, A.; Gruner, S. M.; Janoff, A. S.; Perkins, W. R. Doxorubicin Physical State in Solution and inside Liposomes Loaded *via* a PH Gradient. *Biochim. Biophys. Acta, Biomembr.* **1998**, *1415*, 23−40.
(22) Zhu, L.; Yang, S.; Qu, X.; Zhu, F.; Liang, Y.; Liang, F.; Wang, Q.; Li, J.; Li, Z.; Yang, Z. Fibril-Shaped Aggregates of Doxorubicin with Poly- l -Lysine and Its Derivative. *Polym. Chem.* **2014**, *5*, 5700−5706.
(23) Eksborg, S. Extraction of Daunorubicin and Doxorubicin and Their Hydroxyl Metabolites: Self-Association in Aqueous Solution. *J. Pharm. Sci.* **1978**, *67*, 782−785.
(24) Israelachvili, J.; Ladyzhinski, I. The Physico-Chemical Basis of Self-Assembling Structures. In *Forces, Growth and Form in Soft Condensed Matter: At the Interface between Physics and Biology*; Skjeltorp, A. T., Belushkin, A. V., Eds.; Kluwer Academic Publishers: Dordrecht, 2005; pp 1−28.
(25) Lepeltier, E.; Bourgaux, C.; Rosilio, V.; Poupaert, J. H.; Meneau, F.; Zouhiri, F.; Lepêtre-Mouelhi, S.; Desmaële, D.; Couvreur, P. Self-Assembly of Squalene-Based Nucleolipids: Relating the Chemical Structure of the Bioconjugates to the Architecture of the Nanoparticles. *Langmuir* **2013**, *29*, 14795−14803.
(26) Kholodenko, A. L. Analytical Calculation of the Scattering Function for Polymers of Arbitrary Flexibility Using the Dirac Propagator. *Macromolecules* **1993**, *26*, 4179−4183.
(27) Pedersen, J. S.; Schurtenberger, P. Scattering Functions of Semiflexible Polymers with and without Excluded Volume Effects. *Macromolecules* **1996**, *29*, 7602−7612.
(28) Borisev, I.; Mrđanovic, J.; Petrovic, D.; Seke, M.; Jovic, D.; Srđenovic, B.; Latinovic, N.; Djordjevic, A. Nanoformulations of Doxorubicin: How Far Have We Come and Where Do We Go from Here? *Nanotechnology* **2018**, *29*, 332002.
(29) Bombelli, F. B.; Berti, D.; Almgren, M.; Karlsson, G.; Baglioni, P. Light Scattering and Cryo-Transmission Electron Microscopy Investigation of the Self-Assembling Behavior of Di-C $_{12}$ P-Nucleosides in Solution. *J. Phys. Chem. B* **2006**, *110*, 17627−17637.
(30) Gissot, A.; Camplo, M.; Grinstaff, M. W.; Barthélémy, P. Nucleoside, Nucleotide and Oligonucleotide Based Amphiphiles: A Successful Marriage of Nucleic Acids with Lipids. *Org. Biomol. Chem.* **2008**, *6*, 1324−1333.
(31) Berti, D.; Montis, C.; Baglioni, P. Self-Assembly of Designer Biosurfactants. *Soft Matter* **2011**, *7*, 7150−7158.
(32) Lei, J.; Chen, Y.; Feng, X.; Jin, J.; Gu, J. Electrostatic Potentials of Camptothecin and Its Analogues. *Theor. Chem. Acc.* **2014**, *133*, 1542.
(33) Zhang, G.; Zhang, L.; Yang, D.; Zhang, N.; He, L.; Du, G.; Lu, Y. Salt Screening and Characterization of Ciprofloxacin. Characterization of Ciprofloxacin. *Acta Crystallogr., Sect. B: Struct. Sci., Cryst. Eng. Mater.* **2016**, *72*, 20−28.
(34) Zhao, Z.; Ukidve, A.; Krishnan, V.; Mitragotri, S. Effect of Physicochemical and Surface Properties on *In Vivo* Fate of Drug Nanocarriers. *Adv. Drug Delivery Rev.* **2019**, *143*, 3.
(35) Round, A.; Felisaz, F.; Fodinger, L.; Gobbo, A.; Huet, J.; Villard, C.; Blanchet, C. E.; Pernot, P.; McSweeney, S.; Roessle, M.; Svergun, D. I.; Cipriani, F. BioSAXS Sample Changer: A Robotic Sample Changer for Rapid and Reliable High-Throughput X-Ray Solution Scattering Experiments. *Acta Crystallogr., Sect. D: Biol. Crystallogr.* **2015**, *71*, 67−75.
(36) Pernot, P.; Round, A.; Barrett, R.; De Maria Antolinos, A.; Gobbo, A.; Gordon, E.; Huet, J.; Kieffer, J.; Lentini, M.; Mattenet, M.; Morawe, C.; Mueller-Dieckmann, C.; Ohlsson, S.; Schmid, W.; Surr, J.; Theveneau, P.; Zerrad, L.; McSweeney, S. Upgraded ESRF BM29 Beamline for SAXS on Macromolecules in Solution. *J. Synchrotron Radiat.* **2013**, *20*, 660−664.
(37) Brennich, M. E.; Kieffer, J.; Bonamis, G.; De Maria Antolinos, A.; Hutin, S.; Pernot, P.; Round, A. Online Data Analysis at the ESRF BioSAXS Beamline, BM29. *J. Appl. Crystallogr.* **2016**, *49*, 203−212.
(38) Breßler, I.; Kohlbrecher, J.; Thünemann, A. F. *SASfit* : A Tool for Small-Angle Scattering Data Analysis Using a Library of Analytical Expressions. *J. Appl. Crystallogr.* **2015**, *48*, 1587−1598.
(39) Yesylevskyy, S. O.; Ramseyer, C.; Savenko, M.; Mura, S.; Couvreur, P. Low-Density Lipoproteins and Human Serum Albumin as Carriers of Squalenoylated Drugs: Insights from Molecular Simulations. *Mol. Pharmaceutics* **2018**, *15*, 585−591.
(40) Sousa da Silva, A. W.; Vranken, W. F. ACPYPE - AnteChamber PYthon Parser InterfacE. *BMC Res. Notes* **2012**, *5*, 367.
(41) Frisch, M. J.; Trucks, G. W.; Schlegel, H. B.; Scuseria, G. E.; Robb, M. A.; Cheeseman, J. R.; Scalmani, G.; Barone, V.; Mennucci, B.; Petersson, G. A.; Nakatsuji, H.; Caricato, M.; Li, X.; Hratchian, H. P.; Izmaylov, A. F.; Bloino, J.; Zheng, G.; Sonnenberg, J. L.; Hada, M.; Ehara, M.; Toyota, K.; Fukuda, R.; Hasegawa, J.; Ishida, M.; Nakajima, T.; Honda, Y.; Kitao, O.; Nakai, H.; Vreven, T.; Montgomery, J. A., Jr.; Peralta, J. E.; Ogliaro, F.; Bearpark, M.; Heyd, J. J.; Brothers, E.; Kudin, K. N.; Staroverov, V. N.; Kobayashi, R.; Normand, J.; Raghavachari, K.; Rendell, A.; Burant, J. C.; Iyengar, S. S.; Tomasi, J.; Cossi, M.; Rega, N.; Millam, J. M.; Klene, M.; Knox, J. E.; Cross, J. B.; Bakken, V.; Adamo, C.; Jaramillo, J.; Gomperts, R.; Stratmann, R. E.; Yazyev, O.; Austin, A. J.; Cammi, R.; Pomelli, C.; Ochterski, J. W.; Martin, R. L.; Morokuma, K.; Zakrzewski, V. G.; Voth, G. A.; Salvador, P.; Dannenberg, J. J.; Dapprich, S.; Daniels, A. D.; Farkas, O.; Foresman, J. B.; Ortiz, J. V.; Cioslowski, J.; Fox, D. J. *Gaussian 09*; Gaussian, Inc.: Wallingford, CT, 2009.

DOI: 10.1021/acsnano.9b05303
ACS Nano 2019, 13, 12870−12879